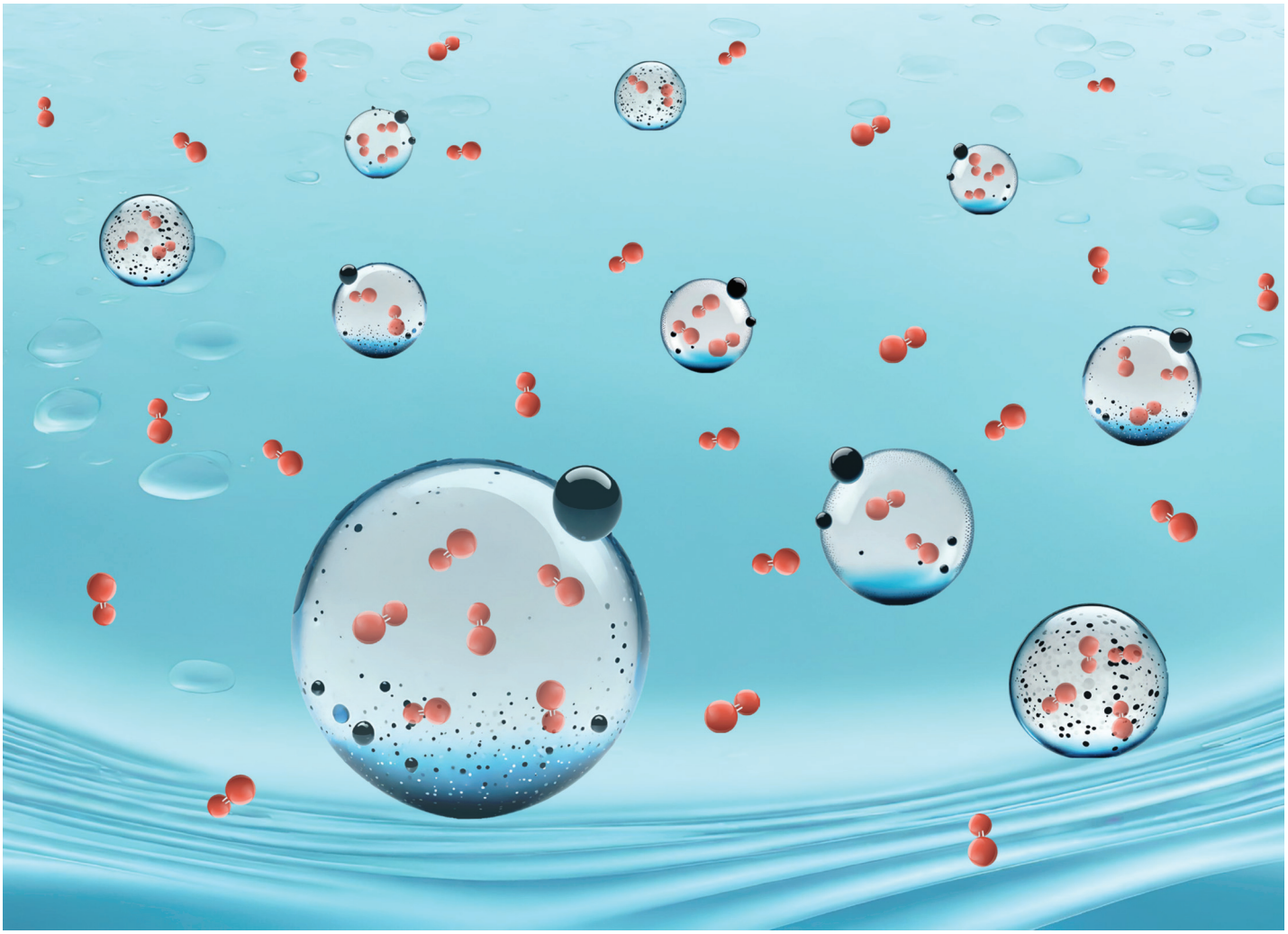

Presenting research from the Department of Advanced Materials Metrology and Life Science at the Istituto Nazionale di Ricerca Metrologica (INRiM), Turin, Italy.

Dual-responsive magnetic nanodroplets for controlled oxygen release *via* ultrasound and magnetic stimulation

A method for decorating ultrasound-sensitive oxygen-loaded nanodroplets with magnetic nanoparticles is reported, to obtain dual-responsive drug delivery nanosystems. A comprehensive analysis of the physicochemical properties of these nanosystems confirms their suitability for oxygen release applications, following the magnetic droplet vaporization induced by alternating magnetic fields. This positions the magnetic nanodroplets as promising candidates for the development of innovative oxygen delivery systems in biomedical fields.

As featured in:

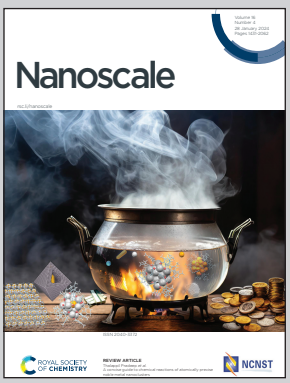

See Simone Galati, Marta Vassallo *et al.*, *Nanoscale*, 2024, **16**, 1711.

ROYAL SOCIETY OF CHEMISTRY

rsc.li/nanoscale

Registered charity number: 207890

Nanoscale

ROYAL SOCIETY OF CHEMISTRY

PAPER

View Article Online
View Journal | View Issue

Cite this: *Nanoscale*, 2024, **16**, 1711

Dual-responsive magnetic nanodroplets for controlled oxygen release *via* ultrasound and magnetic stimulation†

Simone Galati, *‡[a,b] Marta Vassallo,*‡[a,b] Marta Vicentini,[a] Marta Vallino,[c] Federica Celegato,[a] Gabriele Barrera,[a] Daniele Martella,[a,d,e] Elena S. Olivetti,[a] Alessio Sacco,[a] Jessica Petiti,[a] Carla Divieto,[a] Paola Tiberto,[a] Alessandra Manzin[a] and Adriano Troia[a]

Magnetic oxygen-loaded nanodroplets (MOLNDs) are a promising class of nanomaterials dually sensitive to ultrasound and magnetic fields, which can be employed as nanovectors for drug delivery applications, particularly in the field of hypoxic tissue treatment. Previous investigations were primarily focused on the application of these hybrid systems for hyperthermia treatment, exploiting magnetic nanoparticles for heat generation and nanodroplets as carriers and ultrasound contrast agents for treatment progress monitoring. This work places its emphasis on the prospect of obtaining an oxygen delivery system that can be activated by both ultrasound and magnetic fields. To achieve this goal, Fe_3O_4 nanoparticles were employed to decorate and induce the magnetic vaporization of OLNDs, allowing oxygen release. We present an optimized method for preparing MOLNDs by decorating nanodroplets made of diverse fluorocarbon cores and polymeric coatings. Furthermore, we performed a series of characterizations for better understanding how magnetic decoration can influence the physicochemical properties of OLNDs. Our comprehensive analysis demonstrates the efficacy of magnetic stimulation in promoting oxygen release compared to conventional ultrasound-based methods. We emphasize the critical role of selecting the appropriate fluorocarbon core and polymeric coating to optimize the decoration process and enhance the oxygen release performance of MOLNDs.

Received 29th September 2023,
Accepted 27th November 2023

DOI: 10.1039/d3nr04925f

rsc.li/nanoscale

1. Introduction

In recent years, oxygen delivery systems based on nanomaterials have gained interest in developing new therapeutic treatments for hypoxic tissues caused by various diseases, such as cancer, diabetes, and infections.[1–6] Fluorocarbon compounds, which are linear, cyclic or polycyclic fluorine-substituted hydrocarbons, have been identified as ideal candidates for the development of carriers for oxygen release, such as oxygen-loaded nanobubbles (OLNBs) or oxygen-loaded nanodroplets (OLNDs), due to their stability, inertness, and high solubility in stabilizing gas.[7–13] OLNBs and OLNDs differ in their physical state, gas and liquid respectively, depending on the boiling temperature of the fluorocarbon employed for their synthesis.

In the literature, most of the OLNBs and OLNDs that have been tested are based on perfluoropentane (PFP) core and decafluoropentane (DFP) core, respectively. These fluorocarbons are characterized by different boiling points, comprised in the ranges 28–32 °C for PFP and 51–55 °C for DFP.[9] The oxygen release from such systems is based on the acoustic cavitation mechanism, *i.e.* the growth and oscillation of bubbles in a solution under ultrasound (US) field exposure. Depending on the applied acoustic pressure in the solution, cavitation can be stable or inertial. If the pressure is low, cavitation is stable and the bubbles oscillate around their resonant size, allowing for controlled oxygen release. In contrast, if the pressure is high, inertial cavitation occurs, which leads to violent bubble collapse.[14–17]

Liquid formulations of OLNDs have shown a series of advantages compared to OLNBs. Among the others, more efficient performance in the oxygen release has been demon-

[a]*Istituto Nazionale di Ricerca Metrologica (INRiM), Strada delle Cacce 91, Torino 10135, Italy. E-mail: simone.galati@polito.it, marta.vassallo@polito.it*
[b]*Politecnico di Torino, Corso Duca degli Abruzzi 24, Torino 10129, Italy*
[c]*Consiglio Nazionale delle Ricerche (CNR), Strada delle Cacce 73, Torino 10135, Italy*
[d]*European Laboratory for Non-Linear Spectroscopy (LENS), Via Nello Carrara 1, Sesto Fiorentino 50019, Italy*
[e]*Università degli Studi di Firenze, Via della Lastruccia 3, Sesto Fiorentino 50019, Italy*

†Electronic supplementary information (ESI) available. See DOI: https://doi.org/10.1039/d3nr04925f

‡These authors contributed equally to this work.

strated, together with the exhibition of a reduced size profile, potentially allowing them to travel through nanoscaled inter-endothelial gaps, typically found in the fenestrated capillaries associated with tumor environments.[2,9,18] OLNDs can undergo acoustic cavitation after their vaporization into microbubbles (diameter in the range of 10–100 μm) due to the interaction with an energy source, which induces an increase in the local temperature up to the fluorocarbon boiling point. Standard methods for inducing vaporization, such as acoustic droplet vaporization or optical droplet vaporization, use US or optical stimuli.[19,20] However, these conventional approaches present a limited ability to reach deeper target regions of the human body while maintaining controlled side effects. This limitation arises from the dependence of energy source penetrability on the specific properties of the tissues that need to be crossed.[21] A possible solution to overcome this limit is the exploitation of the heat released by the activation of magnetically functionalized OLNDs with radiofrequency magnetic fields, to allow for magnetic droplet vaporization and consequentially to activate the oxygen release.[21,22] The advantage of using magnetic fields as stimuli is that their penetration in the body is not affected by the tissue properties, thus greater penetration depths can be achieved. Magnetic functionalization can be obtained by decorating the OLND surface with magnetic nanoparticles (MNPs), which are able to release heat when excited with alternating current (AC) magnetic fields with frequency typically in the range of 100 kHz–1 MHz. In particular, the field induces a cyclic response of the MNP magnetization configuration, which leads to heat generation, mainly due to hysteresis losses.[23] The capability of MNPs to release heat is generally expressed with the specific loss power (SLP) parameter, which describes the power dissipated per unit mass of magnetic material and can be derived from thermometric or calorimetric measurements.[24]

Recently, there have been a few studies investigating the magnetic droplet vaporization mechanism as well as the functionalization and conjugation processes to obtain hybrid multi-responsive nanocarriers with acoustic and magnetic properties.[25] While some works have explored the application of magnetic droplet vaporization to other theranostic nanosystems, such as heat mediators for magnetic hyperthermia treatment[22] or contrast agents for US imaging,[21] none of these studies have considered the oxygen delivery as a therapeutic mean. On the other hand, particular attention has been paid to the evaluation of *in vitro* biocompatibility, cell internalization, and magnetic hyperthermia efficacy of magnetically decorated OLNDs.[26–30]

In this framework, we focus on the preparation and characterization of magnetic OLNDs (MOLNDs), obtained by decorating OLNDs with Fe_3O_4 nanoparticles (NPs). These hybrid nanomaterials were investigated for the application of magnetic droplet vaporization in oxygen delivery. The synthesis of OLNDs was performed by using two types of fluorocarbon cores, based on PFP or DFP, and two polymers as coating, dextran or chitosan.[17] The Fe_3O_4 NPs were prepared *via* co-precipitation method.[31]

We conducted a comprehensive physicochemical characterization to investigate the impact of Fe_3O_4 NP inclusion on the properties of nanodroplets. Furthermore, we indirectly assessed the effectiveness of the magnetic decoration through two distinct experiments. These experiments involved the examination of magnetic features exhibited by the prepared MOLNDs, scrutinizing whether their streaming velocity and trajectory within solution were influenced by the gradient of a magnetic field generated by a permanent magnet. Subsequently, we evaluated the efficacy of oxygen release under both acoustic and magnetic stimuli, analyzing the different performance of MOLNDs with respect to variations in fluorocarbon core and polymer coating types. The results, particularly in terms of oxygen concentration released *via* the AC magnetic field activation, demonstrated competitive performances compared to the conventional US-mediated method applied to OLNDs.

2. Results and discussion

2.1. Analysis of nanodroplet physicochemical and dimensional properties

Four different samples of OLNDs were synthesized in liquid phase through a sonication procedure, using two different fluorocarbons as core, DFP and PFP, and two different polymers as coating, dextran and chitosan. The oxygen-storing capacity of the samples has been investigated in previous studies, showing a loading of 0.45 mg mL^{-1}.[2,9] For each sample, MOLNDs were obtained through a surface decoration with Fe_3O_4 NPs, as schematized in Fig. 1A. The used Fe_3O_4 NPs, which were previously characterized in terms of physicochemical and dimensional properties,[31] present a quasi-spherical shape and an average size of about 10 nm, forming aggregates with dimensions in the order of 150 nm. Moreover, their magnetization curve demonstrates a dominant superparamagnetic behavior at room-temperature.[32] The prepared OLNDs and MOLNDs were compared after performing an exhaustive characterization of their physicochemical and dimensional properties, through scanning electron microscopy (SEM), transmission electron microscopy (TEM), dynamic light scattering (DLS), and ζ potential analysis (Fig. 1).

Representative SEM images of the marks left by DFP-based nanodroplets with chitosan coating on a silicon wafer after drying are shown in Fig. 1B. In the image of OLNDs (left), it is possible to appreciate quasi-circularly shaped halos with dimensions of a few hundred nanometers, made of the solid residues left on the silicon substrate by the liquid droplets after they collapse and evaporation. In the image of MOLNDs (right), clusters of Fe_3O_4 NPs can be observed in proximity to the droplet halos, as a proof of their localization on the droplet external surface.

Higher resolution images were obtained with TEM, as illustrated in Fig. 1C for DFP-based MOLNDs with chitosan coating. These pictures clearly show the presence of Fe_3O_4 NP aggregates on the nanodroplet surface, confirming the results

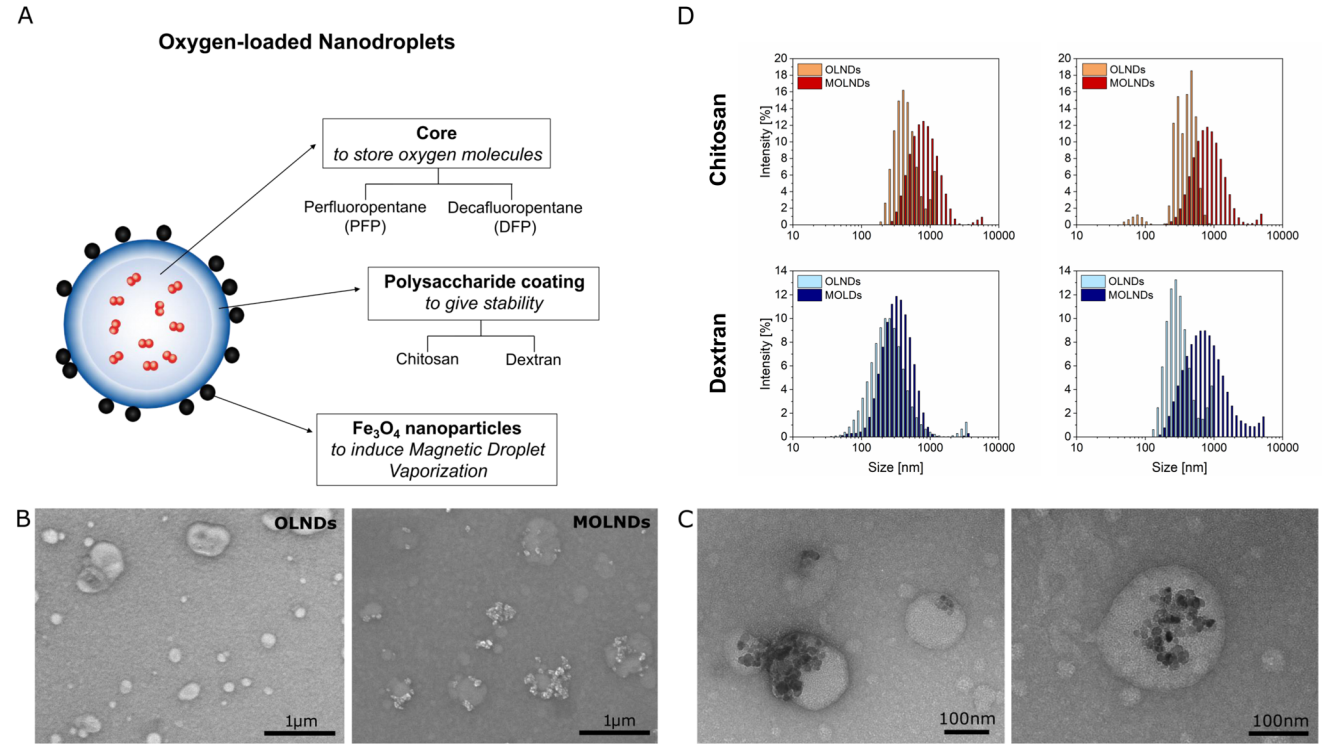

Fig. 1 (A) Schematic representation of MOLND structure. (B) Representative SEM images of the marks left on a silicon substrate by DFP-OLNDs (left) and DFP-MOLNDs (right), both with chitosan coating, after drying. (C) Representative TEM images of chitosan-coated DFP-MOLNDs. (D) DLS size distributions of OLNDs and MOLNDs with different coatings and cores.

obtained with SEM and corroborating the effectiveness of the magnetic decoration.

The histograms of the hydrodynamic size distributions measured with DLS are shown in Fig. 1D and their mean values and standard deviations evaluated over 5 measurements are reported in Table 1. The results indicate that the dimensions of OLNDs with different cores (DFP or PFP) are similar, providing evidence that the fluorocarbon composition does not significantly impact on their size.[2] Conversely, the type of the coating affects the droplet size, as confirmed by the larger diameter of chitosan-coated OLNDs compared to that of dextran-coated ones. Moreover, the surface decoration of OLNDs with Fe_3O_4 NPs is confirmed by an increment in their mean size, regardless of the core and coating employed.

Table 1 also reports the mean ζ potential values and the standard deviations for each sample, evaluated over 5 measurements. The type of coating agent has a strong influence, with dextran resulting in a negative ζ potential, while chitosan in a positive one. Moreover, Fe_3O_4 NPs exhibits a negative ζ potential, which could result in a higher MNP loading level with the chitosan coating due to attractive electrostatic forces resulting from opposite surface charges. Furthermore, the surface decoration with Fe_3O_4 NPs affects the ζ potential, with a decrease in its absolute value for MOLNDs in comparison to their corresponding OLNDs, indicating a lower stability of the suspensions.

Additionally, the OLNDs and MOLNDs acoustic response was investigated by collecting the signal emitted during droplet excitation using US fields, with a passive cavitation detector. The results obtained for the acoustic response of the nanodroplets with DFP-core are shown in Fig. 2, while the ones obtained for the PFP-core are shown in Fig. S1 of the ESI.† Three spectra at increasing acoustic pressures from 0.47 MPa to 1.54 MPa are reported for both OLNDs and MOLNDs in Fig. 2A, where it is possible to observe the acoustic spectra emitted by DFP-core samples, characterized by the increase of harmonics bands, as the ultrasonic pressure at 1.1 MHz increases. These bands are associated with stable cavitation activity related to forced bubble oscillations in the solution.

Table 1 Mean hydrodynamic diameters and ζ potential values of all the studied samples

Sample				Diameter ± σ (nm)	ζ Potential ± σ (mV)
Fe_3O_4 NPs				135 ± 35	−24.8 ± 0.5
OLNDs	Core	Coating	Decoration		
	DFP	Chitosan	✗	419 ± 15	39.5 ± 2.5
			√	627 ± 22	24.7 ± 1.4
		Dextran	✗	285 ± 16	−21.7 ± 3.9
			√	345 ± 15	−18.4 ± 0.3
	PFP	Chitosan	✗	407 ± 11	54.9 ± 2.8
			√	638 ± 21	40.5 ± 1.0
		Dextran	✗	292 ± 12	−50.9 ± 1.8
			√	563 ± 25	−25.6 ± 0.6

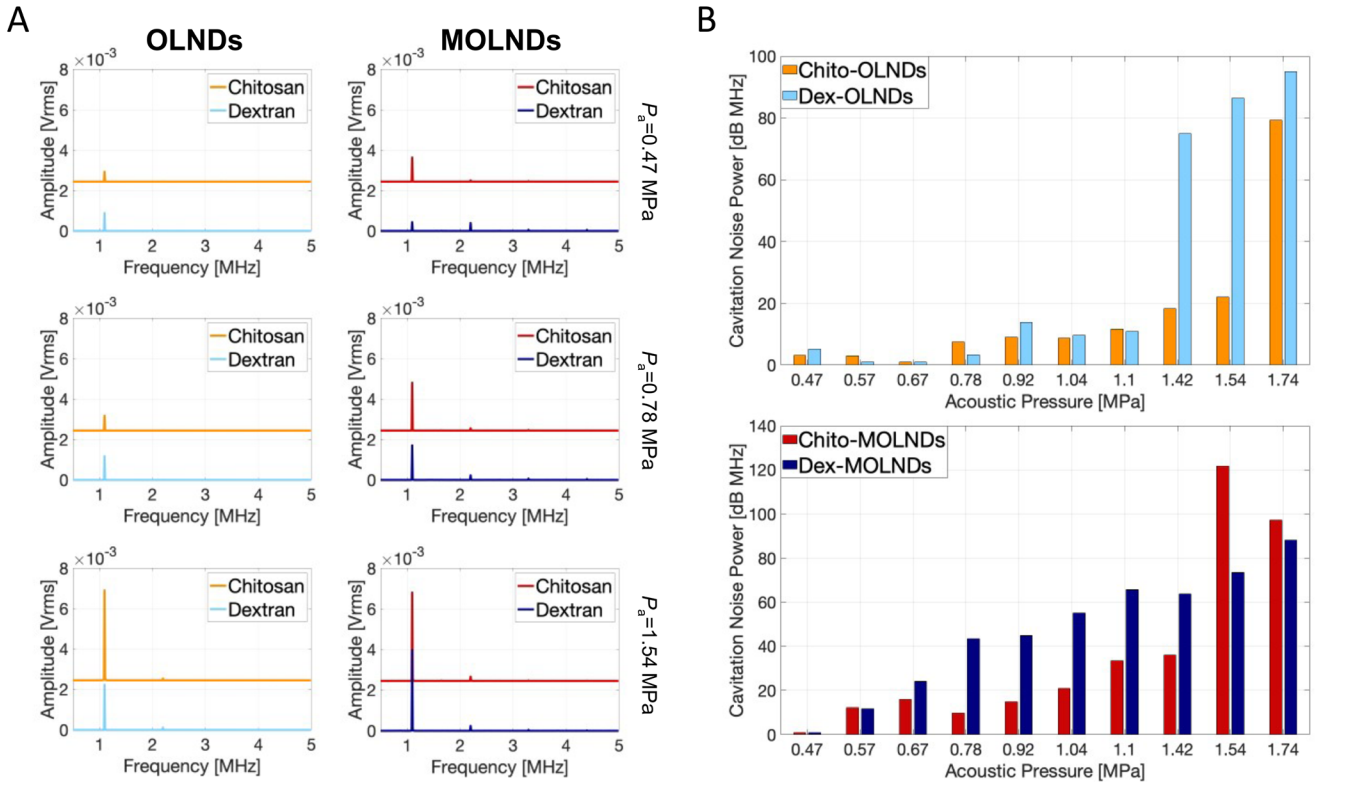

Fig. 2 (A) Acoustic spectra of DFP-core OLNDs and MOLNDs with chitosan and dextran coating, measured at three acoustic pressures (0.47, 0.78 and 1.54 MPa). (B) Cavitation Noise Power (CNP) values evaluated in the acoustic pressure range 0.47–1.74 MPa for DFP-core nanodroplets: comparison between OLNDs (top) and MOLNDs (bottom). The reported results are based on the average of three acquired values.

Interestingly, for MOLNDs there is an increase in the peak amplitude when considering the lowest acoustic pressures (0.47 MPa and 0.78 MPa), indicating a stronger emitted acoustic signal. The different behavior of OLNDs and MOLNDs can be attributed to the presence of Fe_3O_4 NPs in the solution, which enhances the acoustic field scattering events, generating a local increase in pressure and, consequently, in cavitation activity. Thus, the magnetic decoration reduces the acoustic pressure threshold for entering the stable cavitation regime towards lower values. As a result, MOLNDs require lower pressures to enable controlled oxygen release while minimizing the potential side effects associated with high acoustic power. However, this difference is less evident at the highest value of acoustic pressure here considered (1.54 MPa), due to the onset of inertial cavitation events for both samples. To quantify inertial cavitation activity, the acoustic spectra were processed using cavitation noise spectrum analysis, which assumes that the shock waves, generated during bubble collapse produce white noise in the spectrum.[33] The analysis was carried out through the evaluation of the cavitation noise power (CNP) indicator,[33] obtained by first transforming the spectra from linear to logarithmic scale, according to the relationship:

$$I_{\mathrm{dB}} = 20 \cdot \log_{10}\left(\frac{I_{\mathrm{mV}}}{I_0}\right) \quad (1)$$

where I_{dB} is the spectrum amplitude in logarithmic scale, I_0 is the minimum intensity value acquired for each spectrum filtered of all the harmonics and ultra-harmonics components, in order to emphasize white noise contribution, and I_{mV} is the amplitude value acquired in the linear scale. To obtain the CNP indicator, I_{dB} was then integrated over frequency, as follows:

$$\mathrm{CNP} = \int I_{\mathrm{dB}}(f)\mathrm{d}f \approx \sum_{5}^{0.5} I_{\mathrm{dB}}(f)\Delta f. \quad (2)$$

Fig. 2B displays the CNP indicator obtained for the nanodroplets with DFP-core; a large value of CNP means a large acoustic signal generated by inertial cavitation. The results demonstrate that the increase in acoustic pressure causes the CNP to rise after reaching a specific threshold, which varies depending on the type of core and coating. The pressure range before the threshold allows the identification of the optimal working conditions to prevent possible drawbacks from inertial cavitation regime.

Furthermore, the type of coating used affects the cavitation behavior. The chitosan coating provides a more rigid structure compared to dextran, resulting in the triggering of inertial cavitation at higher acoustic pressures for both OLNDs and MOLNDs. Additionally, the magnetic decoration reduces the threshold for the inertial cavitation regime to lower pressures

due to the enhancement of acoustic wave scattering events, as already discussed for stable cavitation.

Similar results are obtained for PFP-core samples, as reported in Fig. S1 in the ESI,† but with more intense signals from both stable and inertial cavitation analysis due to the lower boiling temperature of PFP, thus resulting in a higher percentage of cavitated nanodroplets.

2.2. Analysis of magnetic nanodroplet behavior under magnetic field gradients

The effectiveness of the decoration of OLNDs with Fe_3O_4 NPs was also qualitatively tested by investigating the trajectory of MOLNDs under the effect of a magnetic field gradient produced by a permanent magnet. The presence of the magnet, responsible for a magnetic attractive force on the Fe_3O_4 NPs bound on the nanodroplet surface, affects MOLND trajectory causing streaming velocity variations and deflections. This was demonstrated by conducting two different experiments.

The results obtained from the first experiment are shown in Fig. 3. Through the setup reported in Fig. 3A, MOLNDs were excited by US. Upon interacting with the acoustic field, MOLNDs are pushed towards fixed positions along the acoustic field lines, specifically nodes and antinodes, where they tend to agglomerate.[34] After the US excitation is turned off, the MOLNDs depart from these fixed points. Their trajectories were recorded both in the absence and in the presence of a permanent magnet and used to determine the streaming velocity variations of the MOLNDs.

In Fig. 3B, three subsequent ecographic frames are presented, selected for a clear visualization of the trajectories of the MOLNDs, recorded for the chitosan-coated DFP-MOLNDs in the presence of the magnet (indicated with the red box). These frames provide evidence of the influence of the magnetic field gradient on the MOLND paths. In this case, the MOLNDs experience an enhanced streaming velocity with a preferred direction towards the magnet (as indicated by green and yellow circles), whereas without the magnet, MOLNDs exhibit random motion in all directions (see .GIF file recorded by ecographic probe present in the ESI†).

The average velocities of the DFP- and PFP-core MOLNDs in the same conditions are reported in Fig. 3C. The influence of the magnetic field leads to a significant increase in streaming velocity, at least twice, confirming the previous preliminary evidence and, thus, the successful magnetic decoration for all the samples. Furthermore, these results also point out a difference due to the coating type. In particular, the chitosan-coated MOLNDs are characterized by a higher streaming velocity than the dextran-coated ones, which could be associated with a higher MNP loading. This confirms the presence of electrostatic attraction forces between chitosan coating and Fe_3O_4 NPs, in accordance with the ζ potential values reported in Table 1.

The results obtained from the second experiment are shown in Fig. 4. Fig. 4A schematizes the microfluidic setup

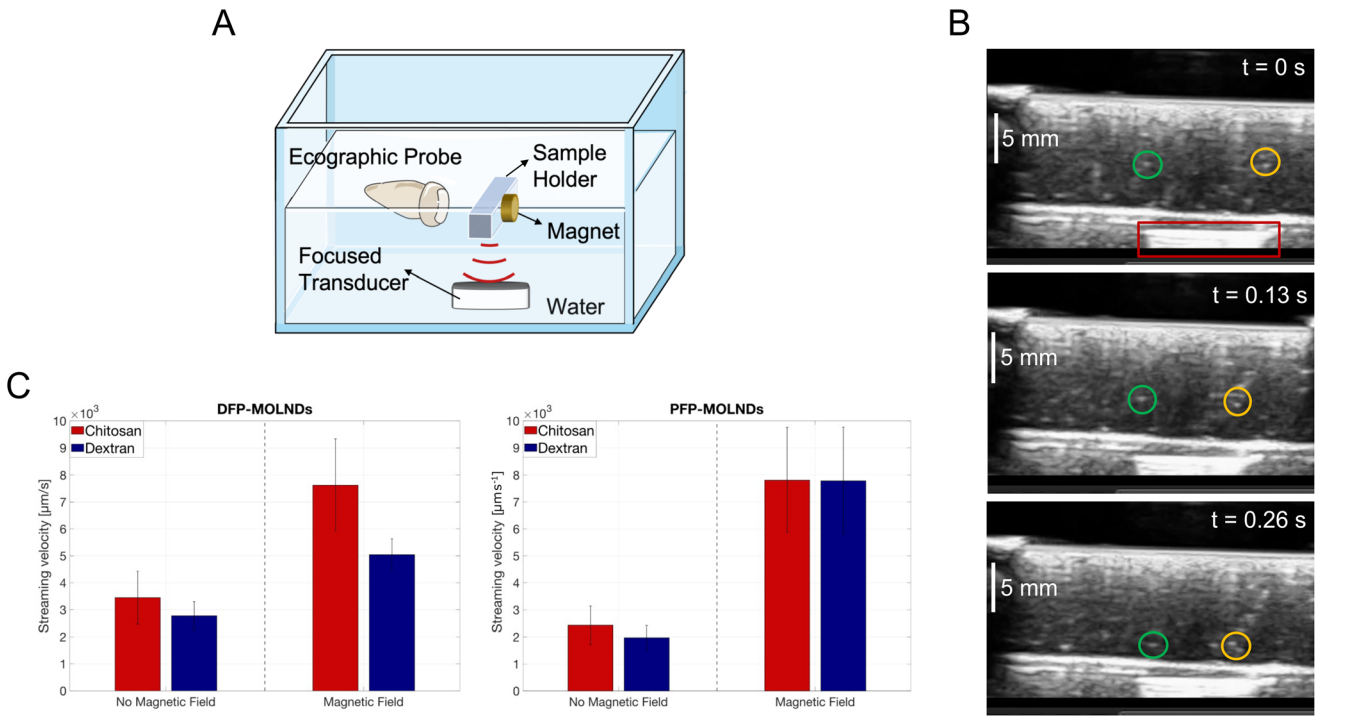

Fig. 3 (A) Schematic representation of the setup used to record the droplet behavior by means of ecographic probe. (B) Frames at three successive time instants, following the US excitation, of the trajectory of chitosan-coated DFP-MOLNDs, under the action of a permanent magnet (red box); green and yellow circles track the droplet movement over time. (C) Average streaming velocities of DFP-MOLNDs (left) and PFP-MOLNDs (right) in presence and absence of the magnet. [The figure was partly generated using Servier Medical Art, provided by Servier, licensed under a Creative Commons Attribution 3.0 unported license].

employed to investigate how the trajectory of MOLNDs is affected by the presence of a permanent magnet, displaced in four different positions with respect to the micro-channel. The deflection angle and the streaming velocity of MOLNDs were extrapolated from the acquired images for each magnet position (Fig. 4B). Fig. 4C and D show the obtained deflection angles and streaming velocities, respectively, for the DFP-MOLNDs. The placement of the magnet laterally to the MOLNDs flow (positions #3 and #4) results in a deflection angle in the investigated frame of approximately 15° from the original trajectory, accompanied by a slight decrease in the average values of the streaming velocity. Conversely, the variations in the deflection angle are not significant in the absence of the magnet or when the magnet is positioned along the flow directions on top of the micro-channel surface (positions #1 and #2). Since the magnet is magnetized out-of-

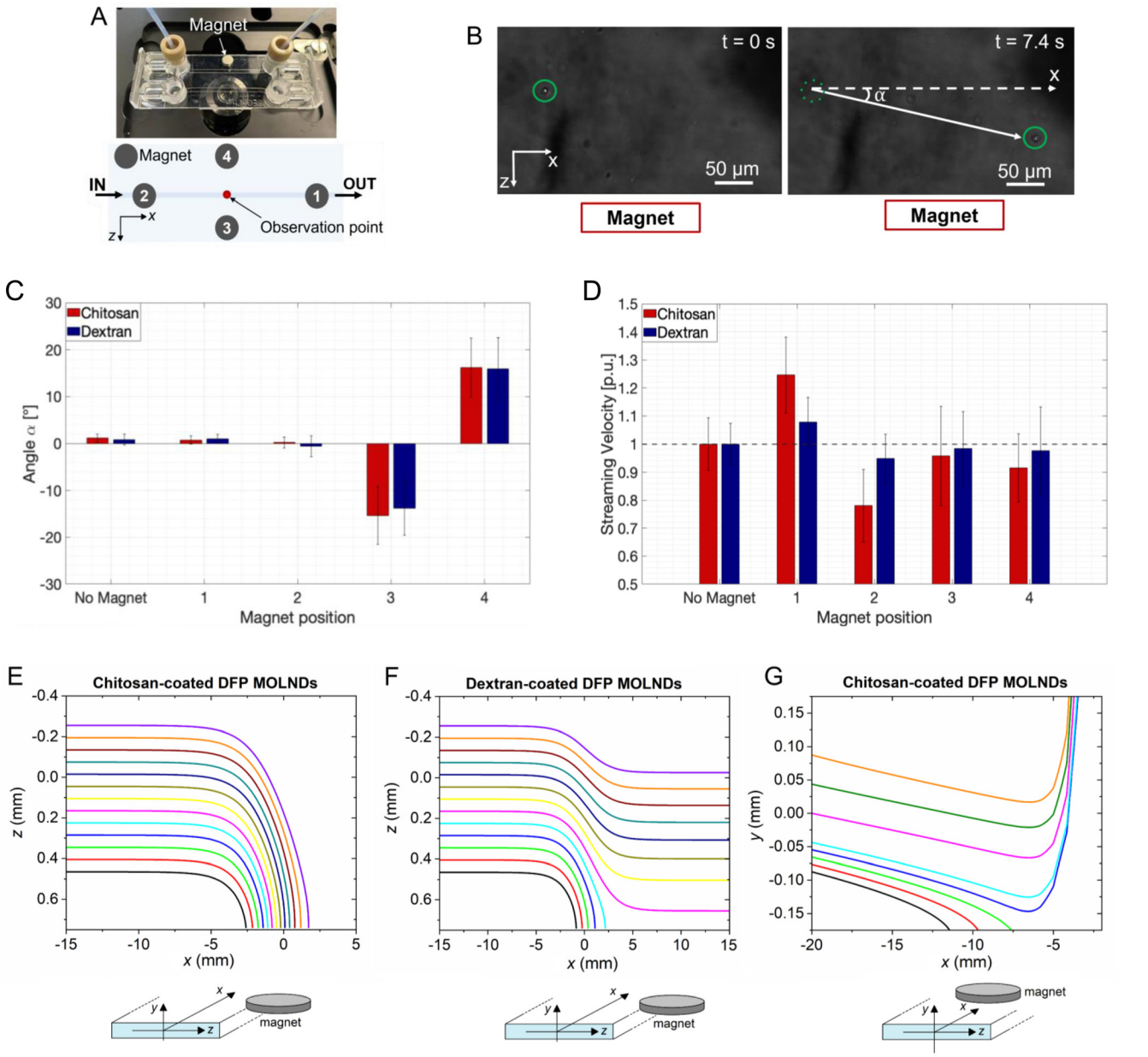

Fig. 4 (A) Picture (top) and schematic (bottom) of the microfluidic setup for investigating MOLND trajectories under the action of a permanent magnet, in four different positions. (B) Frames at two subsequent time instants displaying the trajectory (white continuous arrow) of chitosan-coated DFP-MOLNDs (green circle) under magnet influence. (C) Mean values of deflection angle obtained for DFP-MOLNDs with both chitosan and dextran coating. (D) Mean values of streaming velocity obtained for DFP-MOLNDs with both chitosan and dextran coating, normalized with respect to the 'No Magnet' case. Trajectories in *xz*-plane calculated for (E) chitosan-coated DFP-MOLNDs and (F) dextran-coated DFP-MOLNDs, for magnet position #3. (G) Trajectories in the *xy*-plane calculated for chitosan-coated DFP-MOLNDs, for magnet position #1. In the simulation graphs, the magnet center is positioned at x = 20 mm.

plane, practically no deviations of the MOLND trajectory are indeed expected in the *xz*-plane, but in the *xy*-plane, MOLNDs are attracted by the magnet and thus move towards the channel top surface. When the magnet is positioned after the observation point (position #1), this attraction results in a substantial increase in the streaming velocity, which is approximately 25% for chitosan-coated MOLNDs and 8% for dextran-coated ones (Fig. 4D). For position #2, the streaming velocity is reduced in the observation frame by about 22% for chitosan-coated MOLNDs and 5% for dextran-coated ones. The stronger velocity variations observed for the chitosan-coated samples further confirm their greater MNP loading.

As can be appreciated, the standard deviations of measured deflection angles and streaming velocities are significantly wide. This is a consequence of different aspects: the quite broad distribution of the MOLNDs size (as shown from DLS measurements reported in Fig. 1D); the variations in the magnetic moment of the MOLNDs due to different level of MNP loading; the variable position of MOLNDs when injected within the micro-channel; the strong spatial variation in the magnetic field that rapidly decays with the distance from the magnet. In particular, as depicted in Fig. S2 in the ESI,† the magnetic field amplitude decreases from 25 kA m^{-1} to around 10 kA m^{-1} along the 1.5 mm width channel, corresponding to a magnetic field gradient of 10×10^3 kA m^{-2}.

As illustrated in Fig. 4E–G, the results of the microfluidic experiments were further corroborated by numerical modeling, which allowed us to have a more extended picture of the trajectories of MOLNDs inside the micro-channel, depending on their initial position at the inlet. Due to the considerable variability in the MNP loading level, there is a strong dispersion in the MOLND magnetic moment at saturation. The reported results provide just an illustrative example, assuming for all chitosan- and dextran-coated DFP-core MOLNDs injected in the micro-channel a saturation magnetic moment of 0.042 pA m^2 and 0.0085 pA m^2, respectively. The trajectories calculated in the *xz*-plane when the magnet is located at position #3 are reported in Fig. 4E and F for chitosan and dextran coating, respectively. For the latter, which are characterized by a reduced MNP loading, associated with a lower magnetic moment, the overall trajectories result to be less influenced by the magnet presence. At larger distances from the magnet, the trajectory is slightly deviated, and only the nanodroplets closer to the magnet move towards it. On the contrary, for chitosan-coated MOLNDs, regardless of the initial positions considered, the nanodroplets tend to move towards the channel wall, where the magnet is positioned. In Fig. 4G, we show the simulation results obtained for the chitosan-coated MOLNDs when the magnet is located at position #1. The trajectories in the *xy*-plane put in evidence an opposed action of the magnet and the gravitational force, which results to be dominant for the MOLNDs near the channel bottom surface.

From simulation results, in all cases the deflection angles strongly vary along the trajectory, reaching values in the order of 90° when the MOLNDs approach the magnet. When comparing experimental and modeling results, strong discrepancies can be observed between the measured and calculated deflection angles, and this can be attributed to various factors. Firstly, the evaluation of MOLND trajectories in the experimental analysis is limited to a small observation window (227 × 167 μm), which is only a fraction of the simulated area inside the channel, falling across the curvature of the simulated trajectories. Secondly, the model involves the assumptions of perfectly inelastic collisions, causing the stream of MOLNDs to stop when they collide with the channel wall. Lastly, the simulations assume a uniform distribution of magnetic decoration across the droplet surface (section 6), whereas SEM and TEM images have indicated the presence of MNP agglomerates with diameters around 150 nm.

2.3. Oxygen release and evaluation of magnetic droplet vaporization

The results related to the evaluation of oxygen release of all the samples are reported in Fig. 5, showing the variation of the oxygen concentration measured after the application of the external stimuli. The oxygen release of OLNDs due to the acoustic field inducing an acoustic pressure of 0.13 MPa was recorded using the setup depicted in Fig. 5A, and measurements over time are presented in Fig. 5B, where for each plot the data of oxygen variation were evaluated with respect to the minimum value collected during US exposure. Upon analyzing the different cores, it is notable that for DFP-based OLNDs ($T_{boiling}$ = 51 °C), the oxygen concentration in the solution increases linearly, reaching significant high increments of about 5 mg L^{-1}. In contrast, for the PFP-core, which has a lower boiling temperature ($T_{boiling}$ = 29 °C), the release of oxygen is less evident, and for dextran-coated OLNDs, it begins before the US stimulation, as the vaporization process is being triggered by the ambient temperature. The different behavior between dextran and chitosan coatings could be attributed to the less rigid dextran-based shell.

Fig. 5C depicts the setup used for evaluating the MOLND oxygen release, induced by the heat generated *via* hysteresis losses by the Fe_3O_4 NPs,[23] when exposed to AC magnetic fields. The experiment was performed by applying a magnetic field with a peak amplitude of 72 kA m^{-1} and a frequency of 100 kHz, corresponding to an SLP around 90 W g^{-1} for the considered Fe_3O_4 NPs.[31] The relative oxygen concentration variations measured at discrete temperatures are shown in Fig. 5D. For each temperature condition, the oxygen concentration was for 5 min before the experiment. Then, the sample was exposed to the AC magnetic field until it reached the desired temperature, and the oxygen concentration was assessed for 5 min. The values shown in the graphs represent the oxygen measurement following exposure to the AC magnetic field, as a variation with respect to the initial concentration. Heating curves for some of these temperatures are reported in Fig. S3 in the ESI.† In this case, the different temperatures at which oxygen is released are associated with the core property: for DFP-based MOLNDs, the oxygen concentration does not increase until 45 °C, while for PFP-based ones, it rises significantly starting from 27 °C. This behavior

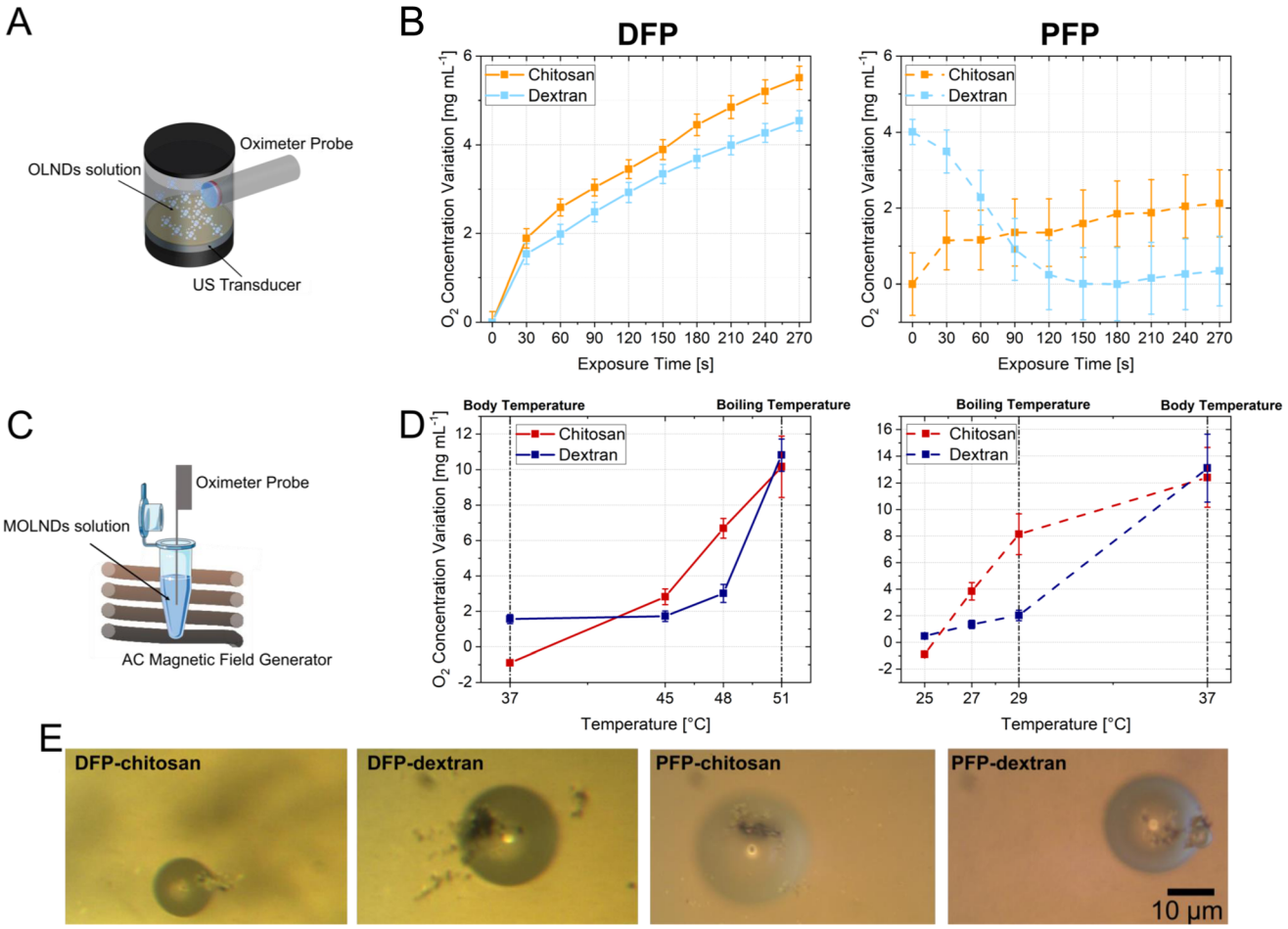

Fig. 5 (A) Visual depiction of the setup used to conduct oxygen release experiments on OLND samples during US exposure (f_0 = 1 MHz, P_a = 0.13 MPa). (B) Variations of the oxygen concentration collected by the oximeter probe during US excitation over time (270 s). (C) Visual depiction of the experimental system to evaluate oxygen release induced by the AC magnetic field stimulus. (D) Variation of oxygen concentration obtained for each MOLND sample at selected temperatures. (E) Optical microscope images of magnetically vaporized MOLNDs. [The figure was partly generated using Servier Medical Art, provided by Servier, licensed under a Creative Commons Attribution 3.0 unported license].

can be attributed to the different boiling points of the two fluorocarbons, even if the temperatures at which oxygen concentration starts to rise are slightly lower than the two boiling points. The reason is that the temperatures in the solution were recorded with a fiber optic probe, which provides a local measure of the temperature in the solution where the sensing point is placed,[35] while on the decorated nanodroplet surfaces (*i.e.* near to the Fe_3O_4 NPs), it results in a higher temperature[36] and thus closer to the actual fluorocarbon boiling point. In terms of coating, chitosan MOLNDs demonstrate significant oxygen release compared to dextran-coated ones. This behavior confirms the higher level of MNP loading shown by the chitosan-coated MOLNDs, as already supported by DLS measurements.

In order to establish the magnetic droplet vaporization role in the oxygen release, the MOLNDs samples were observed with an optical microscope after being exposed to an AC magnetic field with peak amplitude and frequency values as described above, which enable the target temperatures for oxygen release. Fig. 5E displays relevant images of the treated samples, clearly showing that, due to their increased dimensions (in the order of 10–20 μm), the MOLNDs have undergone the process of vaporization. Additionally, aggregates of Fe_3O_4 NPs are visible on the surface of the vaporized MOLNDs, confirming the magnetic decoration responsible for the heating release under the AC magnetic field excitation.

From a qualitative analysis, it is possible to derive the relationship between the temperature achieved in the solution through AC magnetic field excitation and the activation of the vaporization process specific for each sample. In particular, vaporization for PFP-MOLNDs starts around 27 °C, with the appearance of a few bubbles visible in the suspension. Their amount progressively increases with temperature, peaking at 29 °C, and then decreases when overcoming the PFP boiling point. For this reason, only a few bubbles can be observed at 37 °C. A similar behaviour is observed for DFP-MOLNDs, but the vaporization process occurs at higher temperature. In particular, the nanodroplets start to vaporize at 45 °C, reach a

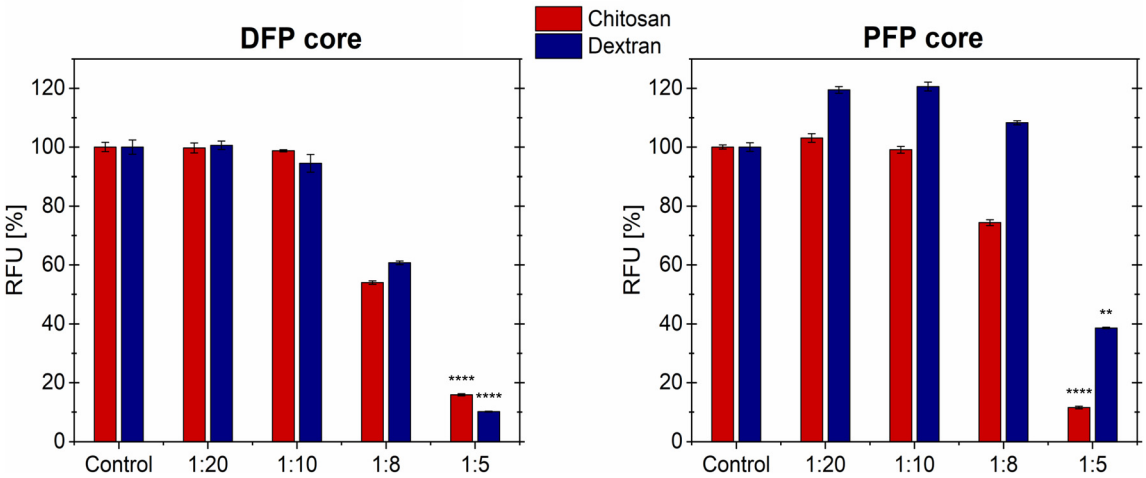

Fig. 6 Cell viability assessment, indicate as percentage of relative fluorescence unit (RFU), on A549 cell cultures after 72-hour incubation with MOLNDs using resazurin assay. Control refers to cells without MOLND treatment, while other cell samples were treated with four different dilutions of MOLNDs (1 : 20, 1 : 10, 1 : 8, and 1 : 5) in the culture medium. The reported data are normalized with respect to the control, which is considered as 100%. RFU data are indicated as mean ± SD (biological replicate no = 3). All the analyses with a p-value < 0.05 were indicated as statistically significant (*$p \leq 0.05$; ** $p \leq 0.01$; *** $p \leq 0.001$; **** $p \leq 0.0001$).

maximum quantity at 48 °C, and start to diminish at 51 °C. Therefore, the different behavior of the DFP- and PFP-MOLNDs is consistent with the boiling temperature of the two fluorocarbons and with the results obtained in oxygen release analysis.

2.4. *In vitro* cytotoxicity studies of magnetic nanodroplets

The cytotoxicity of the DFP- and PFP-core MOLNDs with chitosan and dextran coating was evaluated through *in vitro* assays using A549 human lung cancer cell line. Cell viability was assessed using the resazurin assay. Cells were treated with different dilutions of MOLND suspensions in the culture medium (1 : 20, 1 : 10, 1 : 8, and 1 : 5) for 72 hours (h). Fig. 6 illustrates that cell viability is not reduced for the lowest MOLND concentrations (1 : 20 and 1 : 10 dilutions) for both the DFP- and PFP-cores. Notably, in the case of PFP-core MOLNDs with dextran coating, there is even an increase of nearly 20% in cell viability. However, for the 1 : 8 dilution we observed different behavior based on the composition of the core and coating of the MOLND samples. In particular, cell viability is not affected by the treatment with PFP-core nanodroplets coated with dextran, while a reduction of approximately 20% is noticed in the case of chitosan coating. On the contrary, for the DFP-core MOLNDs a decrease of about 40% in cell viability is observed for both coatings. Lastly, at the highest MOLND concentration (1 : 5 dilution), cell viability drastically decreases within the range of 60–90%. Although the limited number of samples analyzed, these reductions are statistically significant. Intermediate results obtained at 24 and 48 h exhibit a similar trend compared to the 72 h data (Fig. S4 in the ESI†).

3. Conclusions

An optimized method for synthesizing OLNDs and for their magnetic decoration with Fe_3O_4 NPs has been presented, addressing the gap in research for magnetic droplet vaporization as a means for achieving therapeutic oxygen release. Different types of MOLNDs were analyzed, varying their fluorocarbon-based core (DFP or PFP) and their surface coating (dextran or chitosan). The effectiveness of the magnetic decoration process was proved by SEM and TEM characterization, as well as by the investigation of the deflection of the MOLND trajectory under the effect of a magnetic field gradient. We found that the magnetic decoration with Fe_3O_4 NPs affects the acoustic response of all the types of MOLNDs prepared, showing a coherent shift of both stable and inertial cavitation thresholds towards lower acoustic pressures. Magnetic droplet vaporization was studied by exposing MOLNDs to 100 kHz magnetic fields, which promote the release of heat from Fe_3O_4 NPs due to hysteresis losses, as exploited in magnetic hyperthermia.

Furthermore, from our comparative analysis of acoustic and magnetic stimuli for oxygen release, it becomes evident that magnetic droplet vaporization represents a highly promising therapeutic approach, comparable to the established acoustic method. In the reported study, the critical role of selecting the appropriate fluorocarbon core and polymeric coating to optimize the decoration process and enhance the oxygen release performance of MOLNDs is emphasized. In particular, our investigations into different types of cores and coatings have shown that DFP-core MOLNDs are better suitable for biomedical applications at body temperature compared to PFP-based ones due to their higher boiling point. Moreover, the chitosan coating has demonstrated its ability to provide a

more controlled and efficient release of oxygen, thanks to its more rigid structure when compared to dextran.

Finally, our *in vitro* cytotoxicity studies demonstrate that MOLNDs interact non-toxically with A549 cells, particularly when applied at dilutions of 1 : 8 or lower.

These findings provide an encouraging result for the future use of MOLNDs in the biomedical field, as nanocarriers that can release drugs under the application of dual stimuli (magnetic and US fields). Furthermore, their hybrid composition could be promising for the integration of additive theranostic features, like US-based imaging and magnetic hyperthermia.

4. Experiment

4.1. Synthesis of oxygen-loaded nanodroplets

To prepare the liquid formulation of OLNDs, DFP or PFP (1.5 mL), an aqueous solution of polyvinylpyrrolidone (0.5 mL, 0.5%) and a solution (1.8 mL) of Epikuron 200 (1%) and palmitic acid (0.3%) in ethanol were added to deionized water (30 mL) and were homogenized for 2 min at 24 000 rpm in an ice water bath using the Ultra-Turrax SG215 homogenizer. Then, the suspension was saturated with a flow of O_2 for 2 min reaching a final O_2 concentration of 35 mg L^{-1}. At the end, a polymeric solution of chitosan or dextran (1.5 mL, 2.7%) was added dropwise to the mixture during the final homogenization process at 13 000 rpm for 2 min.

4.2. Preparation of magnetic oxygen-loaded nanodroplets

Fe_3O_4 NPs used for OLNDs decoration were synthesized through the co-precipitation method in alkaline environment.[31] Briefly, iron(II) chloride tetrahydrate and iron(III) chloride hexahydrate (Fe^{2+}/Fe^{3+} molar ratio 1 : 2) were dispersed in deionized water and heated up to 75 °C. Then, to promote precipitation, ammonium hydroxide (30%) was added dropwise to reach a pH of 8. The reaction was carried on for 1 h at 85 °C and the resulting precipitate was washed with deionized water and magnetically decanted.

In order to obtain a formulation of MOLNDs, Fe_3O_4 NPs were dispersed in the same solution used for the OLND preparation, without the fluorocarbon compound (DFP or PFP). The mixture was added to the OLNDs suspension in order to reach a final concentration of Fe_3O_4 NPs of 1 mg mL^{-1}. Then, the mixture was sonicated for 20 s in an ice-water bath. This procedure was repeated for all the OLND samples, with PFP or DFP-core and chitosan or dextran coating.

4.3. Physicochemical characterization

The hydrodynamic size distribution and ζ potential of OLNDs and MOLNDs were measured at room temperature by DLS using the Malvern – Zetasizer Ultra instrument. Only values between 110 and 890 nm from the size distributions were considered for calculating the mean hydrodynamic diameter; values outside this range were excluded because they correspond to residual reagents from the synthesis process (<100 nm) and microbubbles that spontaneously vaporize (>900 nm).

SEM images were recorded using the instrument FEI Inspect – F scanning electron microscope through backscattered electron imaging. Prior to the characterization process, a small drop of the suspension was deposited onto a silicon substrate and left to dry completely. This step was crucial in ensuring the sample stability and integrity under the high-vacuum conditions within the SEM chamber.

TEM images were collected with the Philips CM 10 transmission electron microscope, using an electronic beam accelerating voltage of 80 kV. A drop of the suspension was allowed to adsorb for 5 min on a Pelco® carbon and formvar-coated grid, and then rinsed several times with water. The grid was negatively stained with 0.5% w/v uranyl acetate in water and excess fluid was removed with filter paper.

4.4. Characterization of acoustic response

To analyze the acoustic response of nanodroplets, a custom-built setup was utilized, as described in detail below. The US excitation was provided by a focused US transducer (Sonic Concepts H-101) working at a fundamental frequency of 1.1 MHz and driven by an A&R amplifier (model 800A3A), connected with a function generator (Agilent 33250A). Before performing the measurements on the OLNDs and MOLNDs samples, the peak rarefactional pressures were collected through a hydrophone coupled to an oscilloscope (InfiniiVision 2000 X DSO-X 2022A, Agilent Technologies) and stored on a Labview-provided computer, resulting in the range of 0.47–1.74 MPa. The solution was injected through a channel into a customized phantom able to mimic human soft tissue acoustic properties, by using a flow controller (uniPERISTALTICPUMP 1, LLG LABWARE), and the acoustic activity was monitored by means of a focused passive cavitation detector (PCD) for the acquisition of the broadband acoustic signal in the range 0.5–5 MHz. From this analysis, Fast Fourier Transform (FFT) spectra were extracted to determine the acoustic response of the samples; each spectrum was obtained by averaging three acquisitions through Labview.

4.5. Assessment of magnetic decoration

To verify the effective decoration of OLNDs with Fe_3O_4 NPs, we tested the magnetic behavior of the resulting MOLNDs under the action of a magnetic field produced by a permanent magnet, by using two types of setup. The first setup consists of an ultrasonic research scanner (UltrasonixSonixTouch) connected to a linear probe (SA4-/21, Ultrasonix) in the presence or absence of the magnet to analyze OLNDs and MOLNDs. An US (Sonic Concepts SU-103) transducer operating at 3.3 MHz was specifically focused on the center of a sample holder containing the suspension (as shown in Fig. 3A). The sample was exposed to US, and after turning off the excitation, MOLNDs behavior was recorded. Finally, the captured frames were post-processed using the tracking plug-in of ImageJ software,[37] and then the droplet streaming velocity was extrapolated. Each average value was obtained based on 30 measurements. The

used magnet, made of NdFeB, has a disk shape, with a diameter of 12 mm and a thickness of 6 mm, and is magnetized out-of-plane.

The second setup comprises a microfluidic pump (Flow EZ, Fluigent), used to generate a laminar flow within a single micro-channel chip (Be-Flow, BEOnChip), and an optical microscope (IX73, Olympus) connected to an external camera to record the transit of MOLNDs. The micro-channel has a rectangular cross-section with a width of 1.5 mm and a height of 0.375 mm; its length is 43 mm. A solution of MOLNDs is fluxed inside the micro-channel, with a measured inlet and outlet flow rates of, respectively, 11 and 8.5 μL min^{-1}. The trajectory of MOLNDs was monitored in the absence of a permanent magnet as well as by placing it in four different positions with respect to the observation point positioned at the channel center, where the flow rate is considered as the average between the inlet and outlet values (as displayed in Fig. 4A). Both the MOLNDs deflection angle and streaming velocity were evaluated employing the ImageJ software tracking plug-in.[37] Each average value was obtained based on 30 measurements. The used magnet is made of NdFeB and has a disk shape, with a diameter of 5 mm and a thickness of 2 mm, and is magnetized out-of-plane.

4.6. Numerical modeling of magnetic nanodroplet flow under magnetic field gradients

The simulation of the microfluidic flow of MOLNDs under the effect of magnetic field gradients produced by a permanent magnet was performed in two steps. Once discretized the magnet into N hexahedral elements, we calculated the spatial distribution of its stray field numerically integrating the following equation:

$$\mathbf{H}_{\text{magnet}}(\mathbf{r}) = \frac{1}{4\pi}\sum_{i=1}^{N}\int_{\partial\Omega_i}\mathbf{M}_{\text{magnet}}(\mathbf{r}_i)\cdot\mathbf{u}_i\frac{(\mathbf{r}-\mathbf{r}_i)}{\|\mathbf{r}-\mathbf{r}_i\|^3}\mathrm{d}s \quad (3)$$

where $\mathbf{M}_{\text{magnet}}$ is the magnetization vector, $\partial\Omega_i$ is the surface of the i-th hexahedron having normal unit vector $\mathbf{u}_i$ and barycentre with vector position $\mathbf{r}_i$.[38]

Under the assumption of non-interacting MOLNDs and perfectly inelastic collisions with the channel walls, we described the trajectory (*i.e.* the time evolution of the vector position **s** and velocity **v**) of a generic MOLND with mass χ, hydrodynamic radius R_{hyd} and magnetic moment **m** by the following equation:

$$\begin{cases}\chi\dfrac{\mathrm{d}\mathbf{v}}{\mathrm{d}t} = \mu_f(\mathbf{m}\cdot\nabla)\mathbf{H}_{\text{magnet}} - 6\pi\eta_f R_{\text{hyd}}(\mathbf{v}-\mathbf{v}_f) + \mathbf{F}_g \\ \dfrac{\mathrm{d}\mathbf{s}}{\mathrm{d}t} = \mathbf{v}\end{cases} \quad (4)$$

where μ_f, η_f and ν_f are the magnetic permeability, viscosity and velocity of the fluid within the micro-channel, here considered to be water.[39] Neglecting the contribution of the chitosan or dextran coating, the MOLND mass χ was determined as:

$$\chi = \rho_{\text{core}}V_{\text{core}} + \rho_{\text{MNPs}}V_{\text{MNPs}} \quad (5)$$

where ρ_{core} and ρ_{MNPs} are the densities of the MOLND core and of the decorating MNPs. The volumes of the core and of the MNP aggregates were extracted from DLS measurements and observation of SEM/TEM images, assuming as a first approximation that the MNP aggregates form a uniform layer on top of the OLND surface. The gravitational force $\mathbf{F}_g$, taking into account buoyancy effects, was expressed as:

$$\mathbf{F}_g = -[\chi - \rho_f(V_{\text{core}} + \mathbf{V}_{\text{MNPs}})]\mathbf{g}, \quad (6)$$

where ρ_f is the fluid density and **g** is the gravitational force vector.[40]

Under laminar flow conditions, the profile of the fluid velocity amplitude within the channel rectangular cross-section (yz-plane) was approximated as:

$$v_f = v_{f_{\max}}\left[1-\left(\left(\frac{2y}{b}\right)^n\right)\right]\left[1-\left(\left(\frac{2z}{a}\right)^m\right)\right], \quad (7)$$

where $v_{f_{\max}}$ is the maximum fluid velocity, which is reached at the channel center, a and b are the width and the thickness of the channel (with aspect ratio $b/a \leq 0.5$), and parameters $n = 2$ and $m = 1.7 + 0.5(b/a)^{-1.4}$.[41]

In eqn (4), the MOLND magnetic moment was expressed by means of the Langevin function as:

$$\mathbf{m} = M_S\cdot V_{\text{MNPs}}\left[\coth\left(\frac{\mathbf{H}_{\text{magnet}}}{H_0}\right) - \frac{H_0}{\mathbf{H}_{\text{magnet}}}\right] \quad (8)$$

where M_S is the saturation magnetization of the MNPs derived from their magnetization curve, measured with vibrating sample magnetometry,[31] and H_0 is a fitting parameter.[42]

4.7. Evaluation of oxygen release and magnetic droplet vaporization

The evaluation of oxygen release from OLNDs was performed with a digital oximeter (Hach HQ 40D) connected with a luminescent/optical dissolved oxygen probe (LDO 101), placed in a small bath hermetically closed with an US transducer at the base (as shown in Fig. 5A), with a working frequency of 1 MHz resulting in an acoustic pressure of 0.13 MPa. The droplet suspension (5 mL), whose oxygen concentration level was previously collected and used as a reference, was exposed to US excitation for 270 s measuring and storing the oxygen concentration value every 30 s. The MOLNDs oxygen release during the induction of the magnetic droplet vaporization was evaluated with oximeter NEOFOX-GT equipped with a small optical fiber probe (3 mm) from Ocean Insight. The oxygen concentration of each sample was measured both before and after the vaporization process, with the sample holder kept hermetically sealed. Magnetic droplet vaporization was tested by using a custom built setup generating a uniform AC magnetic field with a frequency of 100 kHz and a peak amplitude selectable up to 72 kA m^{-1}.[43,44] A volume of 1 mL of the sample was exposed to the magnetic field, and its temperature was monitored during the exposure using a fiber optic thermometer (Osensa Innovation), as schematized in Fig. 5C. The

magnetic field was turned off once the specific temperatures were reached (from 25 to 37 °C for PFP-core and from 37 to 51 °C for DFP-core). In order to evaluate the occurred vaporization, the samples were observed by an optical microscope (ARISTOMET, Leitz).

4.8. *In vitro* cytotoxicity studies of magnetic nanodroplets

The MOLNDs cytotoxicity was tested *in vitro* on A549 human lung cancer cell line using the resazurin assay, a metabolic assay that evaluates cell viability based on the amount of resazurin converted into resorufin within the cytoplasm of living cells. Fluorescence signal produced by resorufin is directly correlated with the number of viable cells. A549 cell line (ATCC CCL-185) was purchased from the American Type Culture Collection. The cells were cultured in DMEM medium containing 1 g L^{-1} of glucose, without L-glutamine, and with sodium pyruvate (Biowest, France). The culture medium was supplemented with 10% (v/v) heat inactivated fetal bovine serum (FBS) from Sigma-Aldrich (USA), 2 mM of L-glutamine from Lonza (Switzerland), and 1% (v/v) penicillin/streptomycin from Sigma-Aldrich (USA). The cell cultures were maintained in an incubator at 37 °C with 5% CO_2. For the cytotoxicity test, cells were seeded in 48-well plates (15 000 cells per well) and incubated overnight under standard conditions. Subsequently, the cells were treated with MOLNDs samples at four different dilutions in the culture medium (1 : 20, 1 : 10, 1 : 8, and 1 : 5), which were selected to make them comparable to existing studies in the literature.[9,27] Cell viability was assessed after 24, 48, and 72 hours of treatment. A 44 μM solution of resazurin (Invitrogen, Thermo Fisher Scientific, USA) in complete DMEM was freshly prepared before each experiment. After the culture medium was removed, 250 μL of resazurin solution was added to each well, and the cells were incubated for 1.5 h. Then, the metabolized resazurin solution was collected and transferred to a 96-well plate for fluorescence intensity (FI) measurement. FI measurements were performed using the Spark multimode microplate reader (Tecan, Switzerland) using an excitation wavelength (λ_{Ex}) of 545 nm and an emission wavelength (λ_{Em}) of 595 nm, previously optimized in our lab.[45–47] For each experiment, the RFU (Relative Fluorescence Units) was collected. Results from samples treated with MOLNDs were normalized on the control sample (without MOLNDs), considered as 100% viability. Therefore, the results were expressed as a percentage of cell viability relative to the control sample. The data were obtained from three biological replicates. To assess significant differences in cell viability among the sample groups, a one-way ANOVA with Tukey's *post-hoc* multiple comparison test was conducted.

Conflicts of interest

There are no conflicts to declare.

Acknowledgements

SEM images were carried out at QR Labs & NanoFacility Piemonte, at INRiM (NanoFacility Piemonte is supported by the "Compagnia di San Paolo" Foundation). DLS measurements were carried out at the Infrastruttura Metrologica Per la Sicurezza Alimentare (IMPreSA), at INRiM. This work was supported by the Project 18HLT06 RaCHy, which has received funding from the European Metrology Programme for Innovation and Research (EMPIR), cofinanced by the participating states, and from the European Union's Horizon 2020 Programme.

References

1 A. Bisazza, P. Giustetto, A. Rolfo, I. Caniggia, S. Balbis, C. Guiot and R. Cavalli, 30th Annual International IEEE EMBS Conference, 2008, pp. 2067–2070.
2 C. Magnetto, M. Prato, A. Khadjavi, G. Giribaldi, I. Fenoglio, J. Jose, G. R. Gulino, F. Cavallo, E. Quaglino, E. Benintende, G. Varetto, A. Troia, R. Cavalli and C. Guiot, *RSC Adv.*, 2014, **4**, 38433–38441.
3 M. Xavierselvan, J. Cook, J. Duong, N. Diaz, K. Homan and S. Mallidi, *Photoacoustics*, 2022, **25**, 100306.
4 H. Fu, J. Fu, S. Ma, H. Wang, S. Lv and Y. Hao, *J. Mater. Chem. B*, 2020, **8**, 6059–6068.
5 B. Yang, F. Meng, J. Zhang, K. Chen, S. Meng, K. Cai, Y. Zhao and L. Dai, *Nano Today*, 2023, **49**, 101766.
6 H. Fang, Y. Gai, S. Wang, Q. Liu, X. Zhang, M. Ye, J. Tan, Y. Long, K. Wang, Y. Zhang and X. Lan, *J. Nanobiotechnol.*, 2021, **19**, 1–14.
7 H. Lea-Banks, S.-K. Wu, H. Lee and K. Hynynen, *Nanotheranostics*, 2022, **6**, 376.
8 E. G. Schutt, D. H. Klein, R. M. Mattrey and J. G. Riess, *Angew. Chem., Int. Ed.*, 2003, **42**, 3218–3235.
9 M. Prato, C. Magnetto, J. Jose, A. Khadjavi, F. Cavallo, E. Quaglino, A. Panariti, I. Rivolta, E. Benintende, G. Varetto, M. Argenziano, A. Troia, R. Cavalli and C. Guiot, *PLoS One*, 2015, **10**, e0119769.
10 G. Banche, V. Allizond, N. Mandras, N. Finesso, A. Luganini, T. Genova, M. Argenziano, C. Magnetto, G. R. Gulino, J. Roana, *et al.*, *Toxicol. Rep.*, 2022, **9**, 154–162.
11 J. J. Kwan, M. Kaya, M. A. Borden and P. A. Dayton, *Theranostics*, 2012, **2**, 1174.
12 R. Cavalli, A. Bisazza, P. Giustetto, A. Civra, D. Lembo, G. Trotta, C. Guiot and M. Trotta, *Int. J. Pharm.*, 2009, **381**, 160–165.
13 R. Cavalli, A. Bisazza, A. Rolfo, S. Balbis, D. Madonnaripa, I. Caniggia and C. Guiot, *Int. J. Pharm.*, 2009, **378**, 215–217.
14 E. A. Neppiras, *Phys. Rep.*, 1980, **61**, 159–251.
15 R. Pecha and B. Gompf, *Phys. Rev. Lett.*, 2000, **84**, 1328.
16 K. S. Suslick and D. J. Flannigan, *Annu. Rev. Phys. Chem.*, 2008, **59**, 659–683.

17 S. Galati and A. Troia, *Int. J. Phys., Math. Sci.*, 2021, **15**, 57–62.
18 E. Stride and C. Coussios, *Proc. Inst. Mech. Eng., Part H*, 2010, **224**, 171–191.
19 O. D. Kripfgans, J. B. Fowlkes, D. L. Miller, O. P. Eldevik and P. L. Carson, *Ultrasound Med. Biol.*, 2000, **26**, 1177–1189.
20 E. Strohm, M. Rui, I. Gorelikov, N. Matsuura and M. Kolios, *Biomed. Opt. Express*, 2011, **2**, 1432–1442.
21 Z. Teng, R. Wang, Y. Zhou, M. Kolios, Y. Wang, N. Zhang, Z. Wang, Y. Zheng and G. Lu, *Biomaterials*, 2017, **134**, 43–50.
22 J. Wang, W. Zhang, Z. Xie, X. Wang, Y. Luo, W. Jiang, Y. Liu, Z. Wang, H. Ran, W. Song and D. Guo, *Adv. Healthcare Mater.*, 2022, **11**, 2201399.
23 C. L. Dennis and R. Ivkov, *Int. J. Hyperthermia*, 2013, **29**, 715–729.
24 A. Makridis, S. Curto, G. Van Rhoon, T. Samaras and M. Angelakeris, *J. Phys. D: Appl. Phys.*, 2019, **52**, 255001.
25 Ş. H. Şanlıer, G. Ak, H. Yılmaz, A. Ünal, Ü. F. Bozkaya, G. Tanıyan, Y. Yıldırım and G. Y. Türkyılmaz, *J. Pharm. Sci.*, 2019, **108**, 1272–1283.
26 S. A. Ansari, E. Ficiarà, F. D'Agata, R. Cavalli, L. Nasi, F. Casoli, F. Albertini and C. Guiot, *Molecules*, 2021, **26**, 4591.
27 E. Ficiarà, S. A. Ansari, M. Argenziano, L. Cangemi, C. Monge, R. Cavalli and F. D'Agata, *Molecules*, 2020, **25**, 2104.
28 S. Zullino, M. Argenziano, S. Ansari, R. Ciprian, L. Nasi, F. Albertini, R. Cavalli and C. Guiot, *Front. Pharmacol.*, 2019, **10**, 1001.
29 A. Khadjavi, I. Stura, M. Prato, V. G. Minero, A. Panariti, I. Rivolta, G. R. Gulino, F. Bessone, G. Giribaldi, E. Quaglino, R. Cavalli, F. Cavallo and C. Guiot, *Pharm. Res.*, 2018, **35**, 75.
30 W. Song, Y. Luo, Y. Zhao, X. Liu, J. Zhao, J. Luo, Q. Zhang, H. Ran, Z. Wang and D. Guo, *Nanomedicine*, 2017, **12**, 991–1009.
31 M. Vassallo, D. Martella, G. Barrera, F. Celegato, M. Coisson, R. Ferrero, E. S. Olivetti, A. Troia, H. Sozeri, C. Parmeggiani, D. S. Wiersma, P. Tiberto and A. Manzin, *ACS Omega*, 2023, **8**, 2143–2154.
32 Z. Ma, J. Mohapatra, K. Wei, J. P. Liu and S. Sun, *Chem. Rev.*, 2021, **123**, 3904–3943.
33 J. Frohly, S. Labouret, C. Bruneel, I. Looten-Baquet and R. Torguet, *J. Acoust. Soc. Am.*, 2000, **108**, 2012–2020.
34 H. Mitome, Proc. World Congress on Ultrasonics, Paris, 2003.
35 A. Manzin, R. Ferrero and M. Vicentini, *Adv. Theory Simul.*, 2021, **4**, 2100013.
36 S. Merabia, S. Shenogin, L. Joly, P. Keblinski and J.-L. Barrat, *Proc. Natl. Acad. Sci. U. S. A.*, 2009, **106**, 15113–15118.
37 C. A. Schneider, W. S. Rasband and K. W. Eliceiri, *Nat. Methods*, 2012, **9**, 671–675.
38 H. Corte-León, V. Neu, A. Manzin, C. Barton, Y. Tang, M. Gerken, P. Klapetek, H. W. Schumacher and O. Kazakova, *Small*, 2020, **16**, 1906144.
39 M. Vicentini, R. Ferrero and A. Manzin, *J. Magn. Magn. Mater.*, 2020, **513**, 167234.
40 E. P. Furlani, *Materials*, 2010, **3**, 2412–2446.
41 R. K. Shah and A. L. London, *Laminar flow forced convection in ducts: a source book for compact heat exchanger analytical data*, Academic press, 2014.
42 M. Monticelli, A. Torti, M. Cantoni, D. Petti, E. Albisetti, A. Manzin, E. Guerriero, R. Sordan, G. Gervasoni, M. Carminati, G. Ferrari, M. Sampietro and R. Bertacco, *Small*, 2016, **12**, 921–929.
43 M. Coïsson, G. Barrera, C. Appino, F. Celegato, L. Martino, A. P. Safronov, G. V. Kurlyandskaya and P. Tiberto, *J. Magn. Magn. Mater.*, 2019, **473**, 403–409.
44 R. Ferrero, G. Barrera, F. Celegato, M. Vicentini, H. Sözeri, N. Yıldız, C. Atila Dinçer, M. Coïsson, A. Manzin and P. Tiberto, *Nanomaterials*, 2021, **11**, 2179.
45 J. Petiti, S. Caria, M. Pegoraro, L. Revel and C. Divieto, *How to optimize resazurin-based viability assays: A549 cell line case report*, Istituto nazionale di ricerca metrologica technical report, 2023.
46 C. Divieto, L. Revel, G. Sassi and M. P. Sassi, *J. Phys.: Conf. Ser.*, 2013, 012051.
47 C. Divieto and M. P. Sassi, *Future Sci. OA*, 2015, **1**, FSO58.